Dynamic displacement monitoring of long-span bridges with a microwave radar interferometer

Bochen Zhang [a], Xiaoli Ding [a,*], Charles Werner [b], Kai Tan [c,a], Bin Zhang [a], Mi Jiang [d], Jingwen Zhao [c,a], Youlin Xu [e]

[a] *Department of Land Surveying and Geo-Informatics, The Hong Kong Polytechnic University, Kowloon, Hong Kong, China*
[b] *GAMMA Remote Sensing AG, 3073 Gümligen, Switzerland*
[c] *College of Surveying and Geo-Informatics, Tongji University, Shanghai, China*
[d] *School of Earth Science and Engineering, Hohai University, Nanjing, Jiangsu, China*
[e] *Department of Civil and Environmental Engineering, The Hong Kong Polytechnic University, Kowloon, Hong Kong, China*

ARTICLE INFO

ABSTRACT

Structural health monitoring of long-span bridges is a critical process in ensuring the operational safety of the structures. In this paper, we present experimental results of monitoring the displacements of two long-span bridges in Hong Kong Ting Kau Bridge (TKB) and Tsing Ma Bridge (TMB) with a terrestrial microwave radar interferometer named the GAMMA Portable Radar Interferometer (GPRI). A technique for fusing the measurements from two receiving antennas of the radar instrument is proposed. In addition, a two-step phase unwrapping approach is also tested. The results reveal the bridge dynamic responses under different loading conditions, including winds, vehicle traffic, and passing trains. The results also show that the terrestrial microwave radar interferometer can be used to monitor the dynamics of long-span bridges with unprecedented spatial and temporal resolutions.
© 2018 International Society for Photogrammetry and Remote Sensing, Inc. (ISPRS). Published by Elsevier B.V. All rights reserved.

1. Introduction

Urban structures such as buildings, elevated roads, and bridges are essential elements of a city that support the daily lives of the urban population. Urban structures may however displace due to defects in the structural design or construction, disturbance from nearby construction activities, deterioration, and under various loading conditions such as those caused by heavy vehicles, typhoons, or earthquakes. It is vitally important to monitor the health conditions of urban structures, to detect any impending structural problems so that necessary remedial actions can be taken in time.

Monitoring of structural displacement or vibration responses is one of the most important objectives of structural health monitoring (SHM). It is especially significant in the case of large-scale infrastructures, such as long-span bridges, where displacement-causing factors need to be evaluated, including dead load, railway load, highway load, wind load, thermal expansion, and seismic events (Xu and Xia, 2011). Depending on the different observation

scenarios and displacement mechanisms, various types of monitoring technologies have been developed and integrated for health monitoring of major bridges. The monitoring technologies can be classified into two groups, (1) contact sensor technologies (Ko and Ni, 2005; Wong, 2004), e.g. accelerometers, fiber optic sensors, wireless sensors, strain sensors, weight-in-motion systems, displacement transducers, tiltmeters, seismometers, level sensing stations, and global navigation satellite system (GNSS) receivers; and (2) geodetic measurement technologies (Jáuregui et al., 2003; Lazecky et al., 2016; Pieraccini et al., 2006; Psimoulis and Stiros, 2007; Sousa and Bastos, 2013; Werner et al., 2012; Zhang et al., 2016; Zogg and Ingensand, 2008), e.g. robotic total stations (RTSs), terrestrial laser scanning (TLS), close-range terrestrial photogrammetry, spaceborne interferometric synthetic aperture radar (InSAR), and ground-based interferometric radar (GBIR).

Sensor-based network technology is most commonly used for long-span bridge displacement monitoring in civil engineering community. In Hong Kong, a sophisticated SHM system based on this technology entitled Wind And Structural Health Monitoring System (WASHMS) has been developed for continuous monitoring of five major long-span bridges (Wong, 2004, 2007). There is however a drawback in these technologies, that is, they all can gather

---

* Corresponding author.
 E-mail address: xl.ding@polyu.edu.hk (X. Ding).

data from only a very limited number of points, due to the cost and operational issues.

Over the past two decades, satellite InSAR has been widely applied in monitoring ground surface motions in nearly all weather conditions, often with a high spatial resolution and high measurement accuracy (millimeter level) (Ferretti et al., 2000; Hooper et al., 2007; Zhang et al., 2011). Owing to the advantages of the high resolution (up to 1 m) and short revisit time (as short as one day) of the newly launched SAR systems since 2007, such as TerraSAR-X and COSMO-SkyMed, the technology has drawn some attention for the long-term monitoring of the instability of urban structures. However, to date only a very limited number of such studies have been carried out to investigate the feasibility of the technology (Lazecky et al., 2016; Montazeri et al., 2016; Perissin et al., 2012).

GBIR is an innovative radar-based remote sensing technique for generating local-scale (a few square kilometers, with a measurement range of 5–10,000 m) digital elevation models (DEMs) and monitoring millimeter-scale surface changes, with outstanding sampling frequency, high measurement accuracy, and excellent spatial resolution (Monserrat et al., 2014). Since a pioneering test was first carried out on concrete girders by Tarchi et al. (1997), using an outdoor portable SAR system called LISA (linear SAR), GBIR has been successfully deployed to study the deformation of a variety of objects, including landslides, glaciers, snowpacks, volcanos, sinkholes, open-pit mining, and human-made structures (Antonello et al., 2004; Caduff et al., 2015b; Casagli et al., 2009; Intrieri et al., 2015; Pieraccini, 2013; Severin et al., 2014; Voytenko et al., 2015). In these applications, the usefulness and tremendous potential of this promising technique in deformation monitoring have been clearly revealed. In the application of bridge dynamic monitoring, a prototype of the high-speed coherent real aperture radar (RAR) system (Ku-band) was first proposed and tested by Pieraccini et al. (2004), where it was found that the data acquisition sampling rate should be faster than 20 Hz and the radar center frequency should be higher than 10 GHz for millimeter-scale dynamic monitoring. A number of studies (Dei et al., 2009; Gentile, 2009; Liu et al., 2015; Stabile et al., 2013) have been conducted to test the capability in different monitoring scenarios (static, dynamic, and long-term) and survey the deformation behavior in some short-span and medium-span bridges (less than 1000 m) based on a stepped-frequency continuous-wave (SFCW) radar interferometer named Image By Interferometric Survey of Structures (IBIS-S, now updated to IBIS-FS and IBIS-FS Plus).

This paper focuses on remote monitoring of the dynamic displacement responses of two long-span bridges with a new type of multi-mode microwave interferometric radar system named the GAMMA Portable Radar Interferometer (GPRI). The research shows some displacement details of the bridges that have never been seen before.

2. Methodology

2.1. Microwave radar interferometer

In recent years, many different types of microwave interferometric radar systems have been developed for some specific purposes, which can be classified into three main types according to the footprint of the radar beam (Caduff et al., 2015a), (1) narrow pencil-shaped beam by dish antenna, (2) narrow fan-shaped beam by slotted waveguide antenna, and (3) wide cone-shaped beam by horn antenna. Technical specifications of most of the commonly used systems can be found in the review article by Caduff et al. (2015a).

Utilizing the benefits of deformation monitoring with a microwave radar interferometer, a portable RAR system with slotted waveguide antenna—the GPRI—was designed and developed by GAMMA Remote Sensing AG (GAMMA) (Werner et al., 2008). As presented in Fig. 1, the GPRI-II (second generation of GPRI) system consists of six major components (Gamma Remote Sensing AG, 2014): (1) one transmitting and two receiving slotted waveguide antennas (beam widths of 0.4 degrees and 45 degrees in the azimuth and elevation directions, respectively); (2) an antenna tower with a GPS antenna on the top center to provide time information (Coordinated Universal Time, UTC in abbreviation) and geographic coordinates (World Geodetic System 1984, WGS84 in abbreviation), and six adjustable brackets on two sides to allow the antenna elevation angle to be changed between minus and plus 45 degrees; (3) a radio frequency assembly (RFA) mounted on the rotating tower to generate the linear frequency modulation chirp and obtain the range compressed radar echo; (4) an azimuthal positioner which can undertake panoramic scanning (360 degrees); (5) an instrument controller with a computer operating system to control and communicate with the RFA; and (6) a power supply unit with either an alternating current (AC) or direct current (DC) power source.

The GPRI uses the frequency-modulated continuous-wave (FMCW) technique to generate a linear frequency modulation chirp in the frequency range of 17.1 GHz to 17.3 GHz. To obtain a high range resolution, another GBIR system, IBIS-S, is operated according to the SFCW technique. FMCW and SFCW are both based on the continuous-wave method, but feature different ways of frequency modulation. One of the distinct advantages of the FMCW-based radar system is that the image acquisition time is drastically reduced compared with the SFCW-based radar system (Monserrat et al., 2014), which is a great advantage for dynamic deformation monitoring. The range resolution Δd_{sr} of GPRI-II (about 0.75 m with a 200 MHz bandwidth) is determined by the bandwidth B of the radar chirp and speed of light C:

$$\Delta d_{sr} = \frac{C}{2 \cdot B} \tag{1}$$

In the case of the two-dimensional radar image acquisition mode, the azimuth resolution Δd_{az} of GPRI-II (about 6.8 m at 1 km range) is determined by the half power beamwidth Θ_{-3dB} and the slant range distance R of the target (Werner et al., 2008):

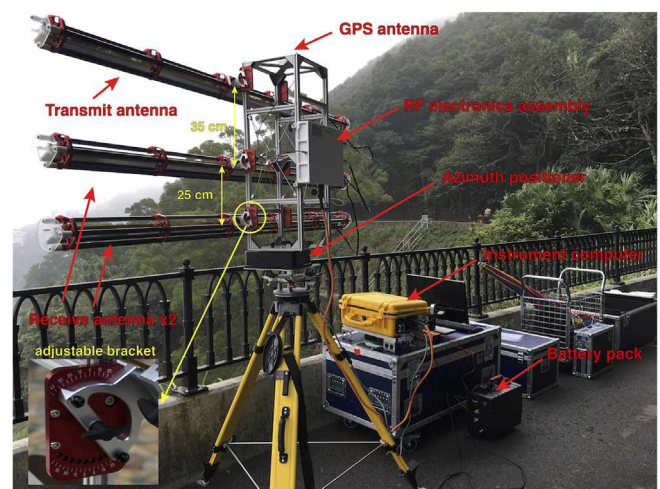$$\Delta d_{az} = \sin(\Theta_{-3dB}) \cdot R \tag{2}$$

Fig. 1. The GAMMA portable radar interferometer (GPRI).

Another key parameter for long-span bridge monitoring is the maximum possible measurement range R_{max} (Werner et al., 2008; Gamma Remote Sensing AG, 2014):

$$R_{max} = k \cdot \tau \cdot f_{max} \cdot \frac{C}{2 \cdot B} \qquad (3)$$

where k is determined by the receiver filter size (a fixed value of 0.9 in GPRI-II); τ is the chirp duration (reciprocal of the sampling rate), which is a function of the number of samples in a chirp N_{samp} and the analog-to-digital converter (ADC) sampling rate f_{ADC} (a fixed value of 6.25 MHz in GPRI-II); and $f_{max} = f_{ADC}/2$ is the Nyquist frequency (also a fixed value of 3.125 MHz in the GPRI-II). The full bandwidth of 200 MHz is generally used, and the maximum measurement range is determined by the chirp duration τ, and directly determined by the number of samples in a chirp N_{samp} in the case of the GPRI-II. Hence, longer-range monitoring can be easily achieved by increasing the chirp duration. For example, the maximum slant range is about 2.109 km with a chirp duration of 1 ms (sampling rate of 1000 Hz), which is long enough and good enough for most long-span bridge monitoring. Some of the other technical characteristics of GPRI-II are summarized in Table 1.

2.2. Ground-based radar interferometry

Ground and satellite-based radar interferometry obeys the same fundamental principles, and only differs in the viewing geometry. In satellite SAR interferometry, the differential interferometric phase is a combination of the systematic phase from the flat term $\Delta\phi_{flat}$, the topographic phase term $\Delta\phi_{topo}$, the deformation phase term $\Delta\phi_{def}$, the propagation phase shift terms, including atmospheric $\Delta\phi_{atm}$ and ionospheric $\Delta\phi_{ion}$ contributions, and the phase noise term $\Delta\phi_{noise}$. After the elimination of the non-deformation induced phase terms from the interferogram, the displacement phase in the radar line-of-sight (LOS) direction can be extracted for the further application in geophysical processes or multi-temporal information extraction. Detailed discussions on this topic can be found in Bamler and Hartl (1998), Ouchi (2013), and Simons and Rosen (2007).

Compared to satellite-based InSAR and the other existing monitoring methods, some of the advantages of GBRI in monitoring human-made structures and a local-scale ground surface can be summarized as follows:

- High measurement precision, excellent spatial resolution, and outstanding temporal resolution. The precision of the deformation measurement $\hat{\sigma}_{d_{LOS}}$ by the use of the GPRI can typically reach a sub-millimeter level along the radar LOS direction (Werner et al., 2012), which is related to the phase noise of the differential interferogram as $\hat{\sigma}_{d_{LOS}} = \frac{\lambda}{4\pi}\frac{1}{\sqrt{SNR}}$ (where λ is the wavelength of the radar signal, $\lambda = 17.4$ mm at 17.2 GHz for GPRI-II; and SNR is the signal-to-noise ratio between two single look complex (SLC) images). The overall deformation for a smaller region can be effectively measured by the GBIR systems, which is a main restriction of the conventional point-wise measurement. Concerning satellite InSAR, GBIR can monitor the deformation with an excellent temporal resolution, e.g. several seconds for 2D (two-dimensional) imaging, and a few microseconds for 1D (one-dimensional) dynamic imaging. For this reason, the decorrelation of radar images caused by the temporal effects can be greatly reduced.

- Optimal observation geometry. The major difference between ground-based and space-based radar interferometry is that the illumination geometry of the former can be chosen according to the site circumstances. Therefore, GBIR can measure effectively structures surrounded by other structures or located in a hilly area while in such cases, space-borne InSAR might be limited by shadowing effect (Stilla et al., 2003). GPS measurements can also be susceptible to multipath effects in addition to the very limited spatial resolution that GPS can usually provide (e.g., Zhong et al., 2008). Additionally, this non-invasive and remotely operated monitoring technique can measure the displacement in areas where the conventional monitoring instruments cannot be installed. The use of GBIR may however also be limited by the measurement geometry. Since only LOS displacements can be measured with the instrument, the measurements are less sensitive to displacements in the other directions. In extreme cases, when the displacements are nearly normal to the LOS direction, it will be difficult to measure the displacements accurately.

- Topography-free interferograms. The interferograms generated by GBIR are obtained from exactly the same position (zero baseline) in general cases, and, consequently, the phase terms of $\Delta\phi_{flat}$ and $\Delta\phi_{topo}$ that are related to the baseline will not exist in most cases of GBIR. In contrast, these phase terms are usually introduced as systematic errors in satellite-based SAR interferometry if the baseline cannot be well estimated. For dynamic GBIR monitoring, the errors related to the spatial baseline are usually negligible. Even though there will be a spatial baseline of a few centimeters in long-term discontinuous GBIR monitoring, the baseline-induced phase terms can be mitigated by fitting in the stable points in the scene, without using an extra DEM (Crosetto et al., 2014; Monserrat et al., 2014). Therefore, the phase terms in ground-based interferometry with a spatial baseline of zero only contribute to $\Delta\phi_{def}$, $\Delta\phi_{atm}$, and $\Delta\phi_{noise}$.

2.3. GPRI in bridge deformation monitoring

In observing a bridge, a GBIR instrument is typically set up near one side of the monitored bridge, looking up toward the bridge deck area, to remotely conduct the near-real-time, short-term, and long-term monitoring. In the application of a small-scale bridge, radar can also be deployed toward the lateral span of the bridge. However, for long-span bridge monitoring, it is not easy to find a suitable view geometry in general applications. After installation of the GBIR instrument, two types of data acquisition, rotated azimuth scanning (RAS) and fixed azimuth scanning (FAS) can be implemented in the long-span bridge deformation monitoring, according to the types of monitoring (near-real-time of the 1D range profile, and short-term or long-term monitoring of the 2D spatial coverage). The displacement field maps are then generated by interferometric processing of the range focused radar
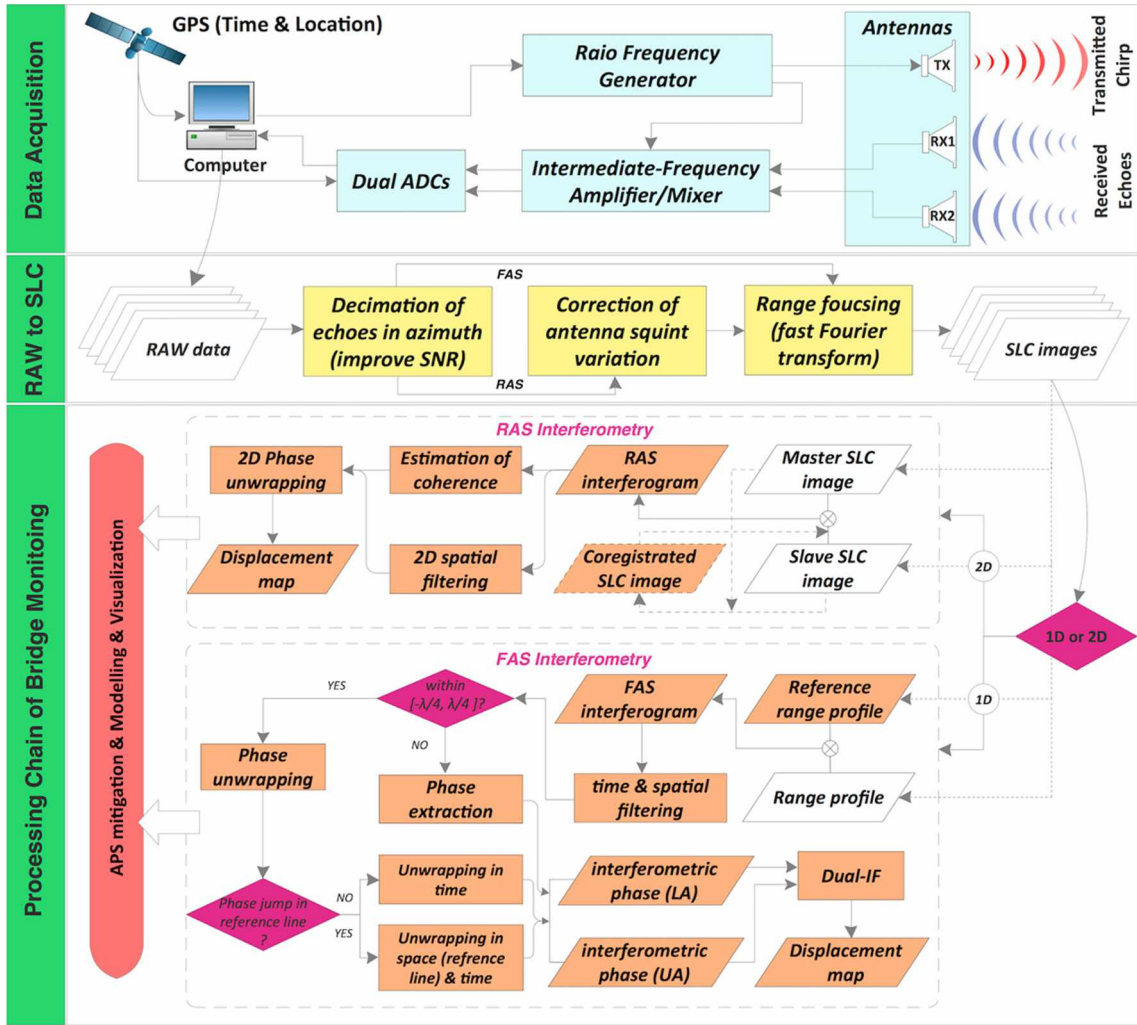
Table 1
Technical characteristics of GPRI-II.

	GPRI-II
Developer	GAMMA
Radar type	FMCW
Antenna type	slotted waveguide
Central frequency	17.2 GHz (Ku-band)
Bandwidth	200 MHz
Polarization	VV
Beam width (horizontal × vertical)	0.4 degrees × 35 degrees
Measurement range	5–10 km
Spatial resolution (range × azimuth)	0.75 m × 6.8 m @ 1 km
Displacement accuracy	less than 1 mm @ 1 km
Maximum sampling frequency[a]	4000 Hz
Radar image product	1D[b] or 2D[c]
Time reference	GPS time

[a] Sampling frequency is a trade-off with the maximum possible measurement range as in (3).
[b] 1D means that the image is a range profile of the focused radar footprint.
[c] 2D means that the product is imaged in both the azimuth and range directions.

Fig. 2. Flowchart of the processing steps.

images, the so-called SLC images. A flowchart depicting the various steps from the data acquisition to the interferometric processing is given in Fig. 2. When generating SLC images from the raw data, azimuth averaging with a factor of 5 to 20 is carried out to improve the SNR of the generated images. The displacement measurements d_{LOS} are the only component of the bridge deformation along the radar LOS direction (see Fig. 3), and they are related to the bridge displacement field of three orthogonal components, d_V, d_{lon}, and d_{lat}, which can be expressed as:

$$d_{LOS} = [d_v \, d_H] \cdot \begin{bmatrix} cos(\theta) \\ sin(\theta) \end{bmatrix} = [d_V \, d_{lon} \, d_{lat}] \cdot \begin{bmatrix} cos(\theta) \\ sin(\theta)cos(\gamma) \\ sin(\theta)cos(\gamma) \end{bmatrix} \quad (4)$$

where d_V, d_H, d_{lon}, and d_{lat} are the bridge displacements in the vertical, horizontal, longitudinal, and lateral directions, respectively. θ is the incidence angle of the radar beam, which is determined by the relative location of the radar and the bridge. γ is the angle between the horizontal displacement vector and the longitudinal displacement vector.

In the RAS mode of the GPRI, the 2D (range and azimuth) radar images are constructed by rotating the antennas in the azimuth around the central axis of the tower. For the GPRI-II, the azimuth
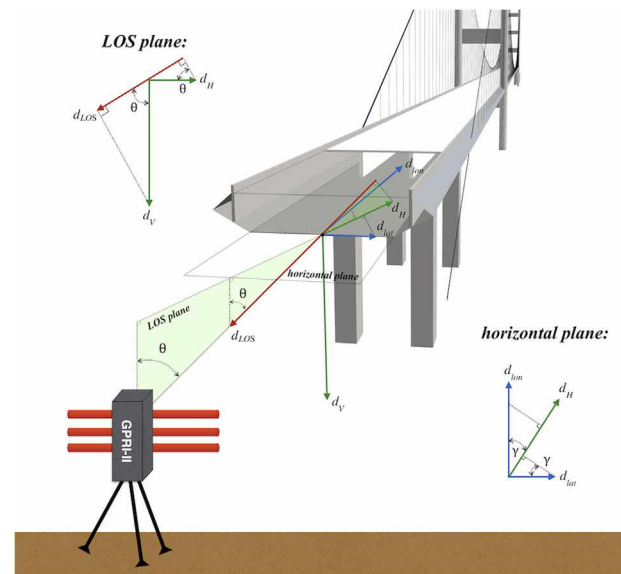

Fig. 3. Illustration of site layout. d_{LOS}, d_V, d_H, d_{lon}, and d_{lat} are bridge displacements in the LOS, vertical, horizontal, longitudinal, and lateral directions, respectively.

positioner can rotate the antennas 360 degrees with steps of 0.1 degrees/second, and can complete the scanning associated with the imaging module. The imaging time of this working mode mainly depends on the sweep angle and the speed of the rotation, and can vary from several seconds to several tens of minutes. The RAS mode can be used to monitor with very high frequency the displacements of almost the entire bridge deck. This working mode also has the potential to detect the possible torsional movements of the bridge using the method proposed by Dei et al. (2009), for which the point-wise-based techniques are inappropriate and limited. 2D imaging with the RAS mode or linear rail based scanning are the most common working modes of many GBIR instruments in large-area and long-term monitoring. The data acquired by the RAS mode can be processed using the "RAS interferometry" processing chain, as shown in Fig. 2, and then analyzed using certain multi-temporal InSAR techniques.

Another advanced working mode of the GPRI is the FAS mode, which is preferable for dynamic structural monitoring. In this working mode, the radar images are constructed in a fixed azimuth look direction, without rotating the antennas. The final product of this working mode is a 1D image only in the range direction over time. The imaging time of the FAS mode depends on the designated ADC capture time for digitizing the signal. Owing to the super-high sampling rate of the GPRI, i.e. up to 4000 Hz, near-real-time deformation monitoring can be implemented for dynamic targets with single points or linear objects. The data processing for the FAS mode is primarily accomplished using the "FAS interferometry" processing chain, as shown in Fig. 2. The main difference between RAS and FAS data processing methods is the basic processing unit: RAS is based on each 2D SLC image, whereas FAS is based on each 1D range profile (azimuth or time profile of the SLC image). Therefore, a critical step for FAS data is to find or generate the reference benchmark for the interferometric process with all the other radar echoes for the specific objective. Usually, the first or averaged range profile is selected as the reference in time in near-real-time bridge monitoring. For some of the small-scale bridges, phase unwrapping is not required with motions in the range of $[-\lambda/4, \lambda/4]$ during the observation (Werner et al., 2012). However, for long-span bridges, the movement or displacement is much more complex, and might exceed that range, so phase unwrapping needs to be performed mainly in the time dimension.

2.4. Two-step phase unwrapping

A simple 1D phase unwrapping can be performed a point by a point in time for the case that the first range profile is used as the reference to generate the interferograms. When the mean range profile is used as the reference, an additional step is used before the 1D phase unwrapping in time, that is, phase unwrapping for the reference range profile of each individual interferograms. In such a case, the first range profile of the interferogram usually cannot be used as the reference for the 1D phase unwrapping in time. A range profile with the minimum root-mean-square (RMS) error to the mean range profile is then selected as the reference. When the bridge displaces rapidly, the neighboring pixels of the reference profile sometimes become incoherent. In such a case, phase unwrapping should be first carried out for the reference profile in the spatial dimension. The 1D phase unwrapping in the time domain can then be performed.

2.5. Dual-antenna image fusion

As introduced in Section 2.1, two receiving antennas are considered in the design of the GPRI system, as this configuration offers more advantages than the monostatic ground-based radar system.

One advantage of this configuration is that the elevation model of the illuminated areas can be quickly reconstructed (Strozzi et al., 2012). Another advantage of this configuration is that it also allows simultaneous monitoring of the deformation with the two generated interferograms. In this section, a dual-antenna interferogram fusion (Dual-IF) method, which benefits from the two receiving antennas, is proposed for the FAS data processing.

The total returned modulations of the incident radar wave for each resolution cell by the upper antenna (UA) and lower antenna (LA) can be expressed as (Oliver and Quegan, 1998):

$$A^u \cdot e^{i\phi^u} = \sum_{k=1}^{N^u} A_k^u \cdot e^{i\phi_k^u} \tag{5-1}$$

$$A^l \cdot e^{i\phi^l} = \sum_{k=1}^{N^l} A_k^l \cdot e^{i\phi_k^l} \tag{5-2}$$

where A^u and A^l are the amplitude of the wave for the UA and LA, respectively; ϕ^u and ϕ^l are the backscatter phase of the wave; A_k^u and A_k^l are the amplitude of the elementary scatterer for the UA and LA, respectively; ϕ_k^u and ϕ_k^l are the backscatter phase of the elementary scatterer; N^u and N^l represent the total number of elementary scatterers within a given resolution cell for the UA and LA, respectively; and $i = \sqrt{-1}$ is the imaginary unit. Due to the attenuations that are caused by the scattering and propagation processes, the received amplitudes of the two antennas A^u and A^l are completely different. The received phases of the two antennas ϕ^u and ϕ^l are both random, and uniformly distributed in $[-\pi, \pi]$, but differ in the time of arrival. Neglecting the noise and atmospheric delay, the propagation time difference Δt of the UA and LA for the same scatterer are almost constant in a very short time period. That is to say, the interferometric phase value of a pixel in the upper interferogram (the interferogram generated by the UA) $\Delta\phi_u$ and the lower interferogram (the interferogram generated by the LA) $\Delta\phi_l$ are, in theory, identical over a very short time period. In practice, however, the noise in both the reference pixels and non-reference pixels may introduce phase discrepancies in $\Delta\phi_u$ and $\Delta\phi_l$. In addition to the noise pixels that are present in both the upper and lower interferograms, the other pixels in the upper and lower interferograms can be integrated using a simple model, as follows:

$$\Delta\phi_{fusion} = \frac{p_u \Delta\phi_u + p_l \Delta\phi_l}{p_u + p_l} \tag{6}$$

where $p_u = 1$ and $p_l = 0$ for the case of systematic biases caused by phase noise in the scatterers of the lower interferogram, and $p_u = 0$ and $p_l = 1$ for the case of systematic biases caused by phase noise in the scatterers of the upper interferogram. The scatterers that are contaminated in both the lower and upper interferograms are masked out before the integration. For the other coherent pixels, p_u and p_l are the coherence values of the upper interferogram and lower interferogram, respectively. Some of the phase discrepancies caused by the residual noise in the non-reference phase will be largely corrected by weighting with the coherence values. $\Delta\phi_u = \phi^u - \phi_{ref}^u$ and $\Delta\phi_l = \phi^l - \phi_{ref}^l$, where ϕ_{ref}^u and ϕ_{ref}^l are the reference phases of the pixels in the upper interferogram and lower interferogram, respectively. The magnitude of coherence $|\widehat{\gamma}|$ is estimated as (Touzi et al., 1999):

$$|\widehat{\gamma}| = \frac{\left|\sum_{i=1}^{L} s_{1,i} s_{2,i}^*\right|}{\sqrt{\sum_{i=1}^{L} |s_{1,i}|^2 \sum_{i=1}^{L} |s_{2,i}|^2}} \tag{7}$$

where s_1 and s_2 are the two zero-mean complex signals; and L is the samples in an estimation window. More detailed information of the coherence estimation can be found in (Hanssen, 2001; Touzi et al., 1999). The detailed procedure of images fusion is described in Section 3.1, and the phase discrepancies are discussed in Section 4.

3. Experimental results

In this section, the two long-span bridges of TKB and TMB in Hong Kong are described to reveal the different types of bridge deformation that are caused by loadings from wind, highway, and railway. For TKB, the study is focused on the deformation due to winds and vehicle traffic. For TMB, the deformation from the passing trains are primarily investigated. The locations of TKB and TMB are shown in Fig. 4(a).

3.1. Monitoring of wind and highway induced deformation of TKB

TKB is a long cable-stayed bridge in Hong Kong, with a span of 1177 m. The bridge links the North-West New Territories to Tsing

Fig. 4. (a) Locations of the two bridges studied. (b) The GPRI set up under the Ting Kau side of the TKB. (c) GPRI set up below the Tsing Yi Tower. (d) Measurement geometry for TKB. (e) Radar intensity image from TKB. (f) Radar intensity image from TMB, where P1, P2, P3, and P4 are the locations of one-half, one-quarter, and one-eighth of the mid-span, and the Ma Wan Tower, respectively. (g) Measurement geometry for TMB, where L, J and H are the locations of GPS stations. Red lines in (e) and (f) show the imaging direction of the FAS monitoring. (For interpretation of the references to color in this figure legend, the reader is referred to the web version of this article.)

Yi Island with a dual three-lane highway. As a part of the Route 3 expressways, it carries one of the heaviest traffic loads in Hong Kong. In this experiment, the radar instrument was deployed under the bridge near the Ting Kau side, with a scanning distance of 80–500 m, as depicted in Fig. 4(d). Both RAS and FAS data acquisition working modes were applied to monitor the bridge deformation due to winds and vehicle traffic. In both scenarios, the radar antennas were looking up at an elevation angle of 30 degrees. Some preliminary results from both the RAS and FAS modes of this test have already been presented in Zhang et al. (2016); however, the results in that paper were generated from only one receiving antenna. In this section, we describe how all the interferograms generated from both the UA and LA with the FAS acquisition mode in the TKB monitoring campaign were processed using the proposed Dual-IF method. A total of 41 radar images were intermittently acquired from 08:05:09 to 08:46:59 (UTC) using 500 μs long chirp and 40 s imaging time. Azimuth averaging with a factor of 20 was carried out to improve the SNR of the radar images, while reducing the sampling rate from 2000 Hz to 100 Hz. However, the reduced sampling rate was still high enough to monitor most of the types of bridge deformation.

Fig. 5(a) and (b) present the original interferograms obtained from the LA and UA at 08:06:10 (the starting imaging time of the radar image), respectively. Due to the LOS direction of the radar being not exactly along the bridge longitudinal direction, as shown in Fig. 4(e), the radar echoes of this monitoring campaign were mainly scattered from the left part of the bridge deck, and the upper-middle part of the main tower. The dense fringes in the left part of Fig. 5(a) and (b) are mainly caused by the deformation of the bridge deck, and the fringes in the mid part of the noisy area are due to vibration of the main tower. After generating the two interferograms from the two antennas, 1D phase unwrapping was performed point-by-point along the time series, and then the pixels with low coherence and intensity were masked out.

Since a high sampling rate was adopted to collect the data in our monitoring, scatterers from the high-scattering materials (with high intensity) of the bridge were all coherent within a very short time period. To avoid the pixels that were contaminated by noise, most of the noisy areas were masked out after the phase unwrapping, and then the outliers in each time slice were removed with a conventional significance level of 0.01.

It was apparent that the interferometric phase measured by the LA was consistent with that measured by the UA in most areas. The differences between the interferometric phases from the LA and UA were significant in some points with diverse noise levels. After the phase unwrapping and noisy pixels masking, this discrepancy also existed in pixels with divergent masking areas, due to the intensity of the SLC images received by the LA and UA being very different, as shown in Fig. 5(c)–(e). Fig. 5(f) presents the difference of the unwrapped phase from the LA and UA. In this study, the unwrapped interferograms from the LA and UA were combined with the proposed Dual-IF method using (6). Firstly, the root-mean-square (RMS) error between the two interferograms was calculated column-by-column to detect the residual phase discrepancy caused by the noise in the reference pixels. From the results, we found that the evident phase discrepancy was only present in the columns with a low amplitude, for either the lower or upper images. For the pixels in these columns with an evident phase discrepancy, we kept the phase values which had a higher mean intensity value. For the pixels that only appeared in the lower or upper interferograms due to the masking, their values were simply maintained in the combined interferogram. For the other pixels in both interferograms, the combined phase value was calculated by weighting with their coherence values. The final fused interferogram is shown in Fig. 5(g). The displacement map can be subsequently produced from the integrated interferogram.

Some selected results from 10 of the 41 displacement maps are presented in Fig. 6, revealing different types of bridge deformation,
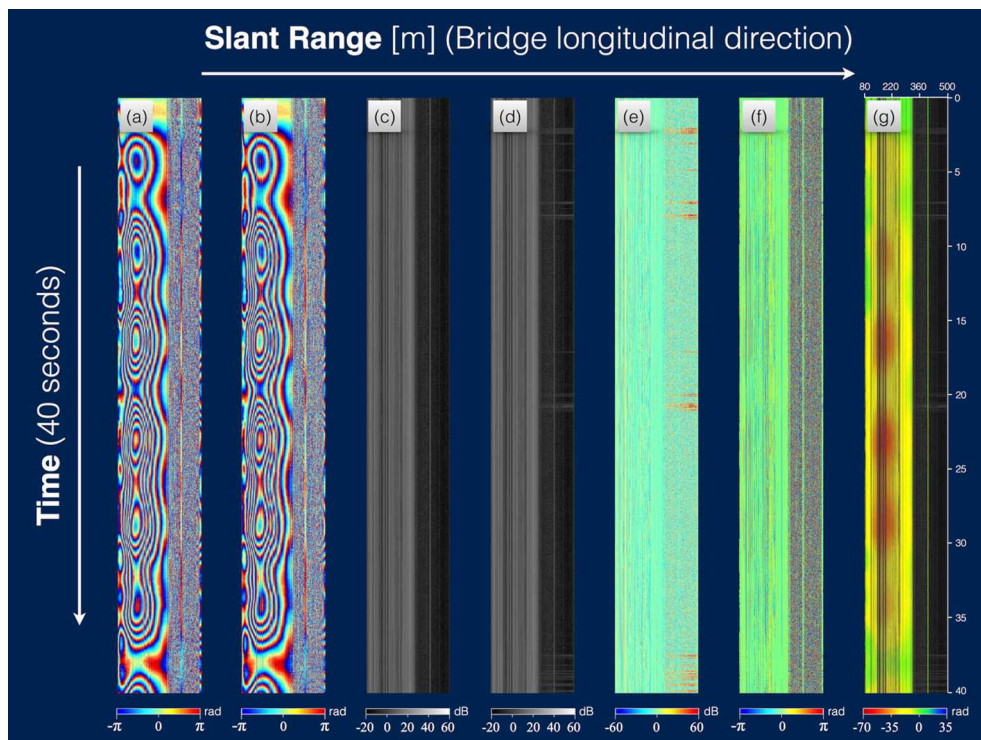

Fig. 5. The results of 080610 (starting time in the format of hhmmss) from TKB. (a) The original interferogram from the LA. (b) The original interferogram from the UA. (c) The intensity image from the LA. (d) The intensity image from the UA. (e) Difference between intensity images from the LA and UA. (f) Difference between unwrapped phase values (rewrapped) of LA and UA without masking. (g) Unwrapped phase from integration of the lower and upper interferograms.
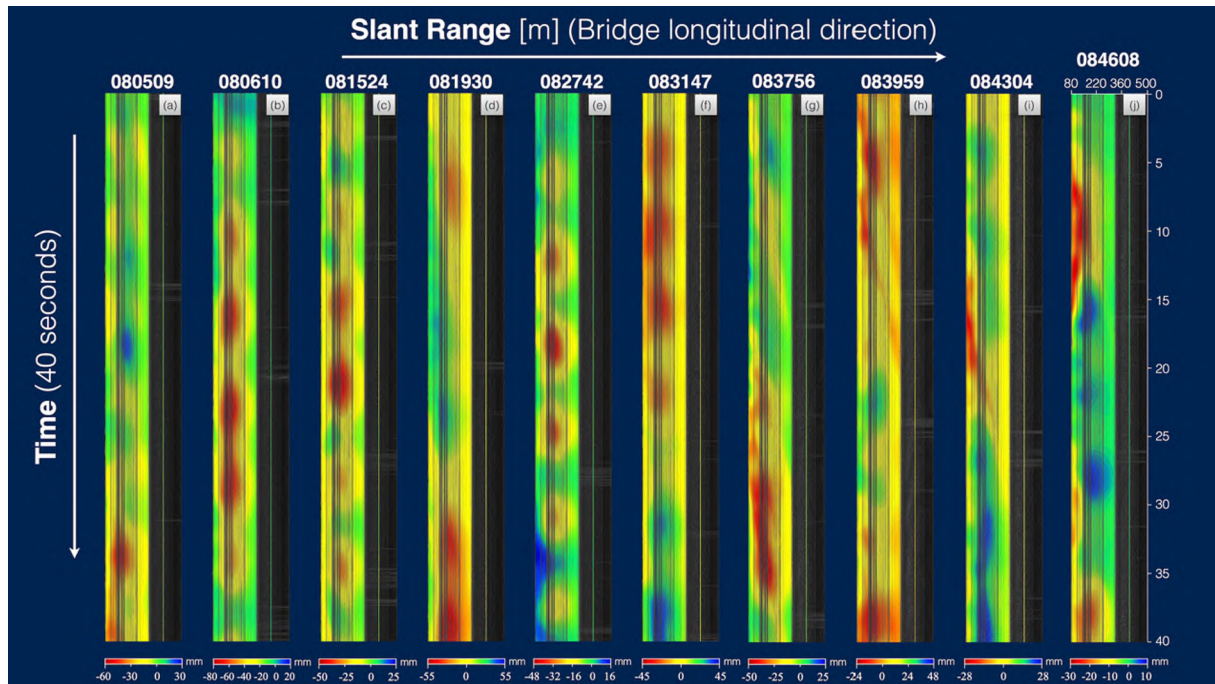
Fig. 6. Samples of displacement maps of TKB.

including natural vibration, motions due to winds, and motions caused by heavy vehicles. The azimuth direction of the figures shows the deformation in the time domain with a time interval of 0.01 s (after azimuth averaging). The high sampling and precision of the measurements have enabled detailed deformation behavior to be revealed. Fig. 6(a)–(f) show mainly that the bridge was moving under different wind conditions. The results also show that the bridge was oscillatory moving with different frequencies in our observation period, and the maximum fluctuation amplitude was around 80 mm. Fig. 7(a) and (b) provide the time series plots of the deformations on the points of the bridge deck and the main tower, from the images of 083147 and 084304, respectively. These two figures indicate that the main tower was relatively stable in our observation period.

Furthermore, even some very small-scale deformations, such as those possibly caused by heavy vehicles as displayed in the top parts of Fig. 6(h) and the middle parts of Fig. 6(i), can be detected from the results of the monitoring. From Fig. 6(g)–(i), it can be seen that the deformation that was possibly caused by the heavy vehicles changed from near-range to far-range over time, which was due to the fact that the left lane of TKB (from the Ting Kau side to the Ting Yi side) is a one-way traffic lane, and all the vehicles in this lane moved from the near-range (Ting Kau side) to the far-range (main tower side) of the radar geometry. In addition, some more detailed information about the deformation possibly caused by the heavy vehicles can also be extracted from the results. As shown in Fig. 6(i), the deformation events that had been possibly caused by heavy vehicles started at about 08:43:17.71 as the vehicles entered our monitoring area, and ended at about 08:44:02.18, with an affected range of 158.912 m in the slant range direction. By assuming that the height between the bridge deck and the transmitting antenna was a constant of 60 m, and the angle between the monitoring direction and longitudinal bridge direction was about 5.6 degrees, the average speed of the vehicles could be calculated, and was approximately 55.76 km/h. The corresponding displacements of the bridge at each moment can also be extracted from Fig. 6(i).
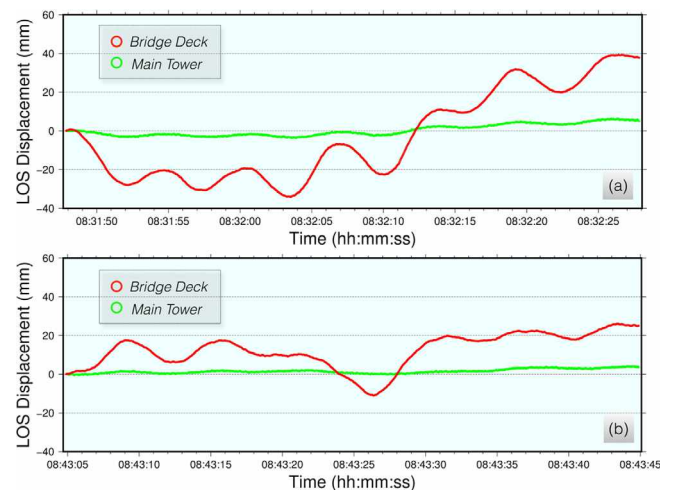

Fig. 7. LOS displacements of two points on the deck and main tower of TKB, from images of (a) 083147 and (b) 084304.

3.2. Monitoring of the railway induced deformation of TMB

Another experimental test in this paper was conducted at TMB, which is a long suspension bridge with a main span of 1377 m. As one of the major transportation facilities in Hong Kong, this bridge is the only route for vehicles and trains traveling between the downtown areas and Lantau Island, with six lanes of highway on the upper deck and two lanes of railway on the lower deck. Compared with TKB, the deformation sources in this observation scenario are much more complex. In addition to the winds and vehicle traffic factors, the deformation caused by the frequently passing trains under the decks makes a major contribution to the bridge motion. In this monitoring campaign, the radar instrument was deployed just below the Tsing Yi Tower on March 28, 2016, as depicted in Fig. 4(g), using the FAS monitoring mode, over a long measurement range of 80–1500 m.
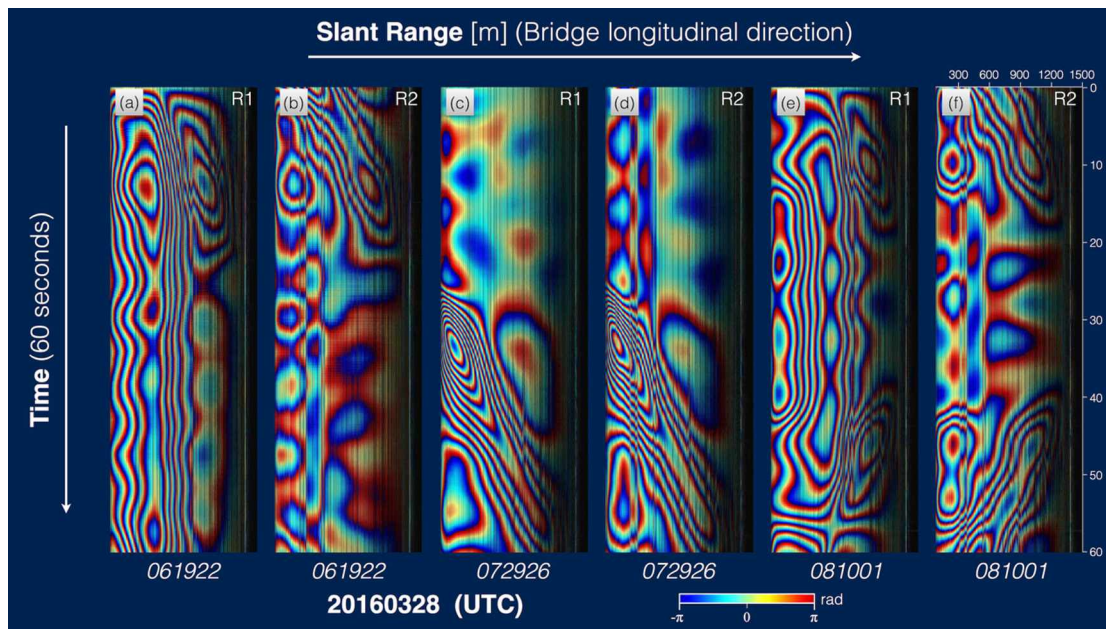
Fig. 8. Interferograms of TMB generated by using two different reference range profiles, (a), (c) and (e) are interferograms generated with the first range profile as the reference while (b), (d) and (f) are interferograms generated with the mean range profile as the reference.

In the FAS monitoring, a total of 104 radar images were intermittently acquired from 06:16:10 to 09:05:15, with 1 microsecond long chirp and 60 s imaging time. The effective sampling rate was about 100 Hz after azimuth averaging, which means that the azimuth (time) direction of the produced radar images had a spacing of 0.01 s. As discussed in Section 2.3, a key step of the FAS data processing is to find or generate the reference signal in time, which determines if the bridge moves upwards or downwards, and the magnitude of the deformation. However, the relative deformation between two time stamps of the same point will not be changed. In the FAS data processing of TMB, the averaged phase value was calculated as the reference signal in time from the radar images that were not contaminated by the deformation caused by the passing trains and the occlusion induced by the massive ships, with a total of 42 radar images and 2,519,580 times repeated measurements. Fig. 8 compares six of the interferograms generated by the use of two different reference benchmarks, i.e. the first range profile of each SLC image ("first line" for short) and the averaged range profile of all the non-contaminated SLC images ("averaged line" for short). The fringes caused by the passing trains are much more distinguishable in the interferograms generated using the averaged line than the first line.

After the two-step phase unwrapping, all the lower and upper interferograms were combined using the proposed Dual-IF method, as same as described in Section 3.1. The bridge displacement fields in the LOS direction from some of the selected results are shown in Fig. 9(a)–(f), which demonstrates three kinds of loading conditions: without a passing train on the bridge, as in Fig. 9 (a); one passing train on the bridge, as in Fig. 9(b)–(c); and two passing rains moving in opposite directions, as in Fig. 9(d)–(f). The displacements vary from the near-range to the far-range in the radar geometry, which means that some trains were moving from Tsing Yi Island toward Ma Wan Island. Whereas, it means that some trains were traveling from Ma Wan Island toward Tsing Yi Island. The maximum LOS displacement was about 90 mm moving toward the radar when only one train passed through the bridge, and the maximum LOS displacement value reached up to 150 mm moving toward the radar when two trains met each other on parallel tracks. It can also be seen that the bridge moved slightly upwards at one side of the bridge (in space) when trains were mov-

ing on the other side, in almost all cases. The time histories of the LOS displacements at four points (near one-half, one-quarter, and one-eighth of the mid-span, and the lower part of the Ma Wan Tower) of the results shown in Fig. 9(a)–(f) are set out in Fig. 10. For the deformation caused by the passing trains, the planar displacements d_{lon} and d_{lat} make little contributions to the radar derived LOS displacements d_{LOS} in most cases, and are only present in some particular cases, such as non-uniform motions of the trains, irregularities at the wheel-to-rail interface, and the centrifugal load on the curved movement path (Xu and Xia, 2011). Thus, it is recommended to neglect the longitudinal d_{lon} and lateral d_{lat} displacement components when monitoring railway induced deformation on bridges that can be regarded as not having planar displacements. With an assumption that the height between the bridge deck and the radar was a constant of 52.378 m (roughly estimated from the results of the laser scanning), the bridge displacement fields in the vertical direction of the TMB experimental results were easily converted with the slant range distances, as shown in Fig. 9(g)–(l). The corresponding transient vertical displacements of TMB at certain moments are depicted in Fig. 11, including without a passing train on the bridge, with only one train on the bridge, and with two passing trains on the bridge. To quantitatively assess results of the TMB displacement induced by railway loadings, we use the statistical results from the historical monitoring by GPS stations in Xu and Xia (2011) as the reference. The maximum downward vertical displacements of GPRI observations are coincidence with the results of GPS in both situations of only one train on the bridge and two trains meet on the bridge as shown in Fig. 11.

4. Discussion

In monitoring long-span bridges, the vertical displacements d_V are usually more significant than the horizontal displacements d_H, including the longitudinal displacements d_{lon} and the lateral displacements d_{lat}. To convert the LOS displacements d_{LOS} into the vertical direction, one possible approach is to neglect the horizontal displacements d_H. This is possible in some cases such as for
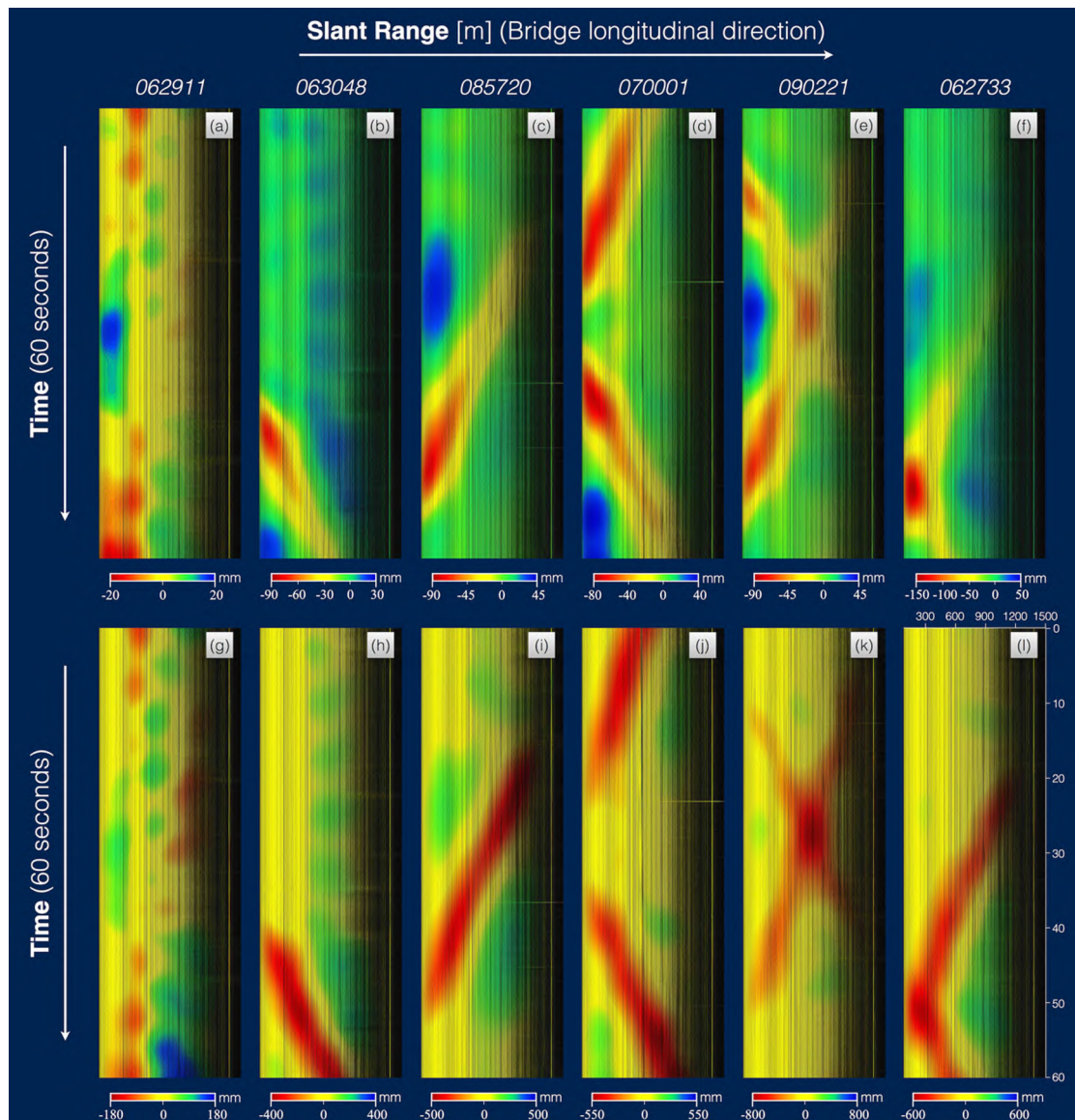
Fig. 9. Displacement maps of TMB, (a)–(f) LOS displacements and (g)–(i) vertical displacements.

deformation caused by passing trains, since the longitudinal displacements are only caused by the acceleration or deceleration of trains (Xu and Xia, 2011), and the lateral displacement contributions are only a small portion of the radar derived LOS displacements, due to the geometry of the monitoring. However, since the elevation difference between radar and the bridge deck is usually very small compared to the bridge length, the look vector of radar in the far-range is almost parallel to the bridge deck. The vertical displacements of the bridge farther away from the instrument are less accurate. Another possible solution is two GBIR systems working together at the same or opposite sides of a bridge, in a similar way to three-dimensional (3D) InSAR (Hu et al., 2014). In addition, sensors on the bridge could also be applied to model the horizontal motions and help to resolve the vertical displacement.

The selection of the reference measurements for generating the interferograms is important. Either the first scan or the mean results from all the scans can be used. The advantage of using the first scan is that the displacement results will be continuous in both time and space, after only 1D phase unwrapping in the time dimension. This method is applicable for some small-scale bridges

with slow motions. To find a reference scan that is not heavily influenced by bridge loadings is, however, often difficult for long-span bridges. The improper selection of the reference scan will lead to misinterpretation of the results. The experiment at TMB illustrates the difference between using the first scan and the averaged results. The assumptions of using the averaged results are that the noise of each pixel is Gaussian distributed, and the bridge motions are discretely sampled in time for as long as possible. As discussed in Section 2.3, a phase unwrapping step is often required for long-span bridge monitoring. Depending on the selection of the reference scan, two types of phase unwrapping strategies can be considered. For the first experiment at TKB, 1D phase unwrapping was only performed in the time dimension. All the results of the experiment were referenced to each pixel itself in the spatial dimension. For the experiment at TMB, the two-step phase unwrapping was applied to generate the displacement field maps, which means 1D unwrapping in the time dimension and an additional unwrapping of the reference line in the spatial dimension. The pixel at the bottom half of the Ma Wan Tower was selected as the reference point for the 1D unwrapping in the spatial dimension. Since the lower part of a bridge tower is usually quite stable, we assumed
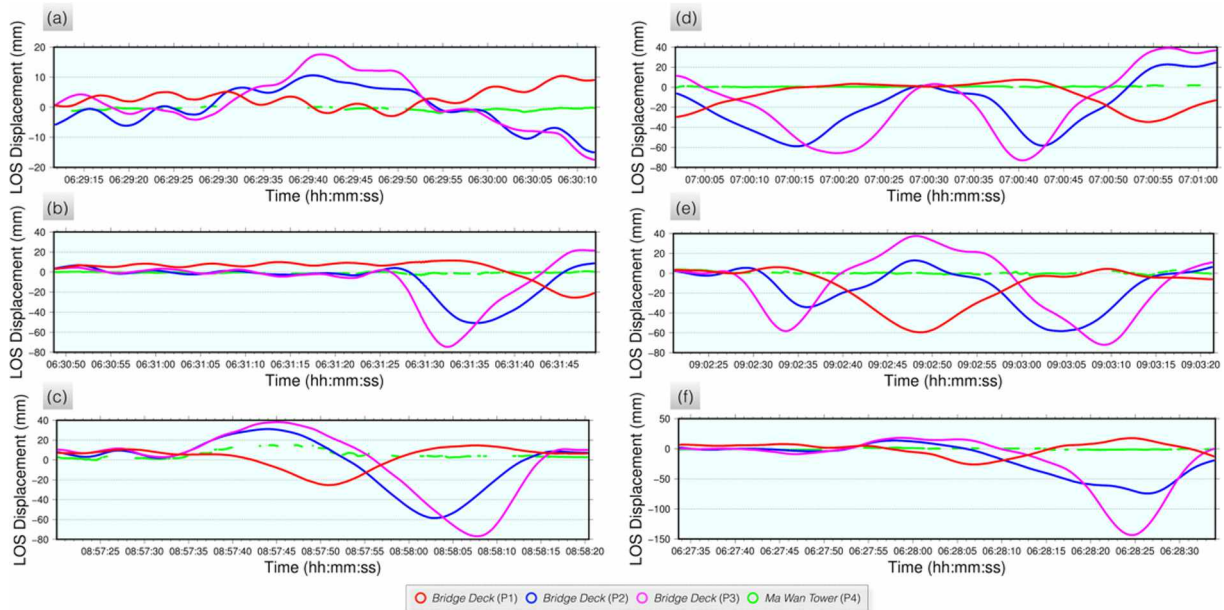
Fig. 10. LOS displacements of four selected points (near one-half, one-quarter, and one-eighth of the mid-span, and the lower part of Ma Wan Tower, respectively, see Fig. 4 (f)) calculated from interferograms in Fig. 9(a)–(f).
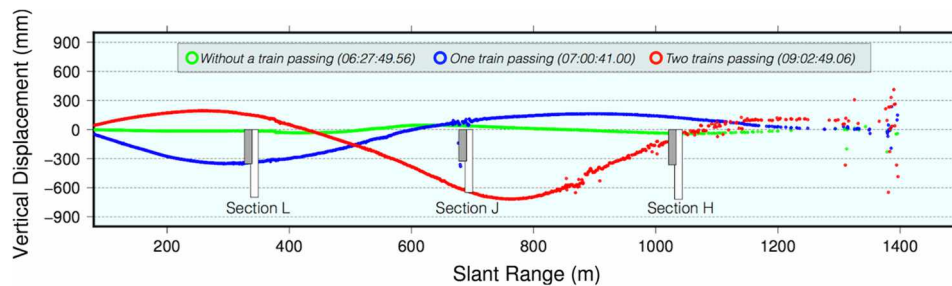

Fig. 11. The vertical displacements of TMB at 06:27:49.56 (without train passing on the bridge), 07:00:41.00 (with only one train on the bridge), and 09:02:49.06 (with two trains on the bridge), respectively. The grey and white bars show the maximum downward vertical displacements from GPS measurements (Xu and Xia, 2011), when one train arriving at and two trains meeting at the locations of the GPS stations on the bridge.

that there were no phase jumps on that pixel between the time of the observation and the time of the averaged line. Therefore, all the results from TMB are referenced to the pixel of the Ma Wan Tower in the space, and the averaged results. However, if there is no "stable" pixel within the observation scenario, the phase shift of the reference pixel between the time of the observation and the time of the reference scan should be calibrated using a given value provided by another technique, such as GPS stations on the bridge. The phase delay caused by the inhomogeneous troposphere is one of the critical issues for the phase-based measurement techniques, including both satellite InSAR (Ding et al., 2008) and ground-based radar (Luzi et al., 2004). For dynamic bridge monitoring using GBIR, the objective is to analyze the effect of the dynamic loadings on the bridge. Thus, the observation time for this objective is usually very short, i.e. several seconds to a few hours. The troposphere might be considered as a homogeneous medium over such a short time period. Therefore, the tropospheric delays may be considered largely canceled out during the interferometric processing for millimeter level monitoring. However, for sub-millimeter level monitoring, the effect of tropospheric delays for dynamic monitoring should be comprehensively investigated further (Iannini and Guarnieri, 2011; Rodelsperger, 2011).

To examine the phase discrepancies between LA and UA images, we look at examples from three different types of scatterers, strong

scatterer, distributed scatterer and noisy scatterer, as shown in Fig. 12(a)–(c). The original interferometric phases and the intensities of the scatterers are presented in Fig. 12(d)–(f) and (g)–(i), respectively. First, the differences are marginal for the strong scatterer as shown in Fig. 12(a). This type of scatterers are dominant for the TMB. In the case of TKB, this type of scatterers is less dominant. The advantage of fusing the two images is not obvious for this types of scatterers although this can enhance the precision. Second, the differences become obvious over certain short time periods for the distributed scatterers as shown in Fig. 12(b). This type of scatterers is common at the monitored bridges. There are three different strategies in processing such data, (1) keeping only the results from one of the antennas that has persistently high intensity over the observation period, (2) making use of the measurements from both antennas but using coherence values as the weights of the measurements, or (3) masking out the scatterers when their RMS value between the two antennas exceed a threshold value. Finally, the scatterers are noisy over majority of the observation period as shown in Fig. 12(c). This type of scatterers should be removed before the Dual-IF method is applied. Fig. 12(j) shows the differences in the displacements of all the scatterers estimated from the two antennas for time period that is the same as for Fig. 5. The results demonstrate that the differences between the two antennas increase when the noise level of either antenna becomes high.
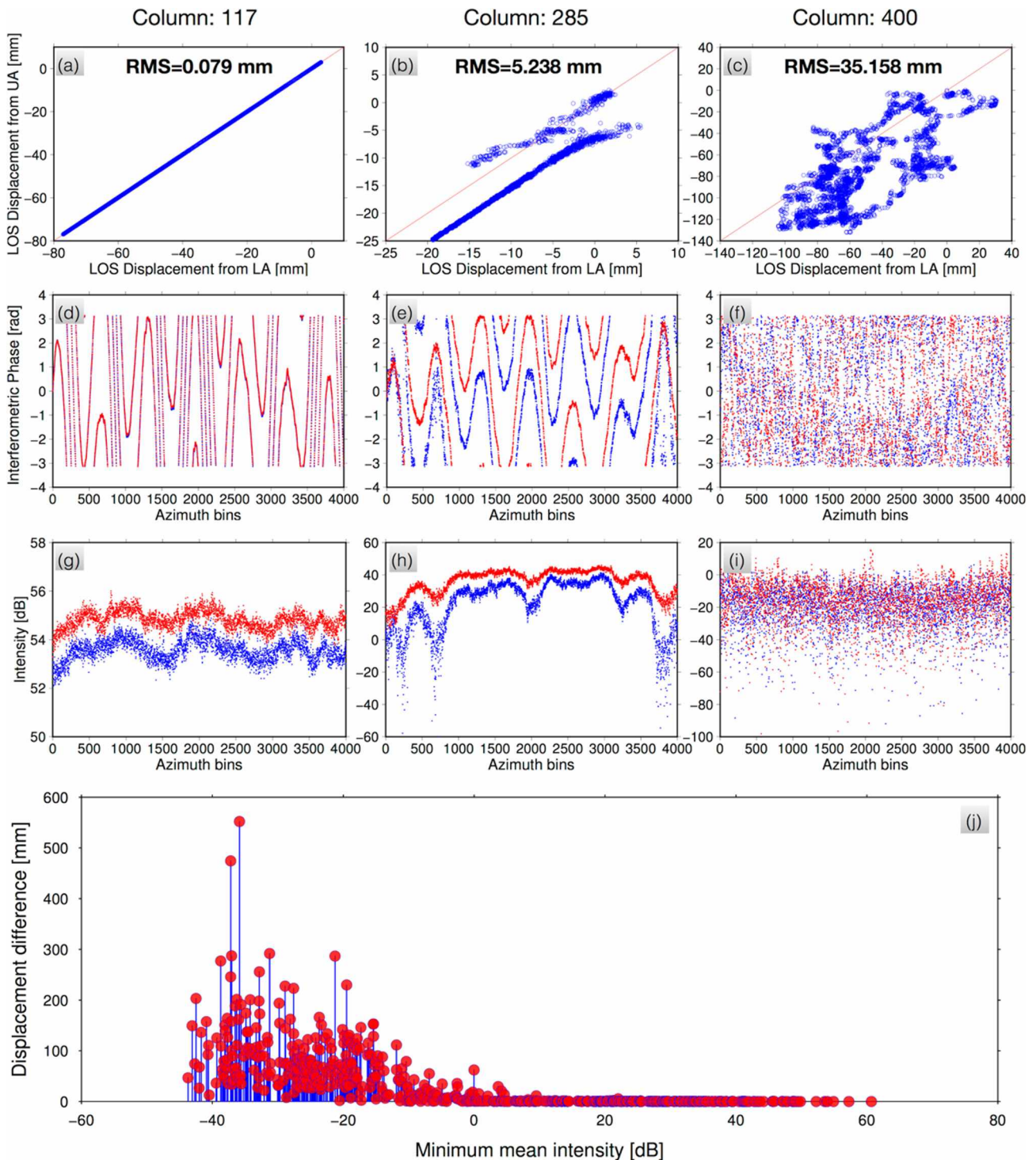
Fig. 12. The phase differences between LA and UA for three different types of scatterers on TKB at 080610, (a) at a persistent scatterer, (b) at a distributed scatterer, and (c) at a noisy scatterer. The corresponding original interferometric phase and intensity values from LA (blue dots) and UA (red dots) are presented in (d)–(f) and (g)–(i), respectively. (j) The relationship between the displacement differences of the scatterers and the minimum mean intensity values of the scatterers in both of the antennas. (For interpretation of the references to color in this figure legend, the reader is referred to the web version of this article.)

5. Conclusions

This paper has described experiments of monitoring the dynamics of long-span bridges using a microwave radar interferometer. Benefiting from the two receiving antennas of the GPRI, a dual-IF method has been proposed to determine the dynamics of the bridges. The results from the proposed method are more robust than those from a single antenna, mainly due to the phase bias caused by the phase noise. The experimental results from TKB in Hong Kong have revealed that the displacements are principally due to winds and vehicle traffics while the results from TMB are mainly related to the passing trains. The study has shown that the GBIR is a very useful technology for monitoring the dynamics of mega bridges, providing unprecedented spatial and temporal resolutions.

Acknowledgements

References

Antonello, G., Casagli, N., Farina, P., Leva, D., Nico, G., Sieber, A., Tarchi, D., 2004. Ground-based SAR interferometry for monitoring mass movements. Landslides 1, 21–28.

Bamler, R., Hartl, P., 1998. Synthetic aperture radar interferometry. Inverse Probl. 14, R1–R54.

Caduff, R., Schlunegger, F., Kos, A., Wiesmann, A., 2015a. A review of terrestrial radar interferometry for measuring surface change in the geosciences. Earth Surf. Proc. Land. 40, 208–228.

Caduff, R., Wiesmann, A., Bühler, Y., Pielmeier, C., 2015b. Continuous monitoring of snowpack displacement at high spatial and temporal resolution with terrestrial radar interferometry. Geophys. Res. Lett. 42, 813–820.

Casagli, N., Tibaldi, A., Merri, A., Del Ventisette, C., Apuani, T., Guerri, L., Fortuny-Guasch, J., Tarchi, D., 2009. Deformation of Stromboli Volcano (Italy) during the 2007 eruption revealed by radar interferometry, numerical modelling and structural geological field data. J. Volcanol. Geoth. Res. 182, 182–200.

Crosetto, M., Monserrat, O., Luzi, G., Cuevas-González, M., Devanthéry, N., 2014. Discontinuous GBSAR deformation monitoring. ISPRS J. Photogramm. Remote Sens. 93, 136–141.

Dei, D., Pieraccini, M., Fratini, M., Atzeni, C., Bartoli, G., 2009. Detection of vertical bending and torsional movements of a bridge using a coherent radar. NDT E Int. 42, 741–747.

Ding, X., Li, Z., Zhu, J., Feng, G., Long, J., 2008. Atmospheric effects on InSAR measurements and their mitigation. Sensors 8, 5426–5448.

Ferretti, A., Prati, C., Rocca, F., 2000. Nonlinear subsidence rate estimation using permanent scatterers in differential SAR interferometry. IEEE Trans. Geosci. Remote Sens. 38, 2202–2212.

Gamma Remote Sensing AG, 2014. GAMMA Portable Radar Interferometer Model: GPRI-II. User Manual (12–August–2014), Gümligen, Switzerland.

Gentile, C., 2009. Radar-based measurement of deflections on bridges and large structures: advantages, limitations and possible applications, IV ECCOMAS Thematic Conference on Smart Structures and Materials (SMART'09), Porto, Portugal, 13–15 July, pp. 1–20.

Hanssen, R.F., 2001. Radar Interferometry: Data Interpretation and Error Analysis. Kluwer Academic Publishers, Dordrecht, The Netherlands.

Hooper, A., Segall, P., Zebker, H., 2007. Persistent scatterer interferometric synthetic aperture radar for crustal deformation analysis, with application to Volcán Alcedo, Galápagos. J. Geophys. Res. 112, B07407.

Hu, J., Li, Z., Ding, X., Zhu, J., Zhang, L., Sun, Q., 2014. Resolving three-dimensional surface displacements from InSAR measurements: a review. Earth Sci. Rev. 133, 1–17.

Iannini, L., Guarnieri, A.M., 2011. Atmospheric phase screen in ground-based radar: Statistics and compensation. IEEE Geosci. Remote Sens. Lett. 8, 537–541.

Intrieri, E., Gigli, G., Nocentini, M., Lombardi, L., Mugnai, F., Fidolini, F., Casagli, N., 2015. Sinkhole monitoring and early warning: an experimental and successful GB-InSAR application. Geomorphology 241, 304–314.

Jáuregui, D.V., White, K.R., Woodward, C.B., Leitch, K.R., 2003. Noncontact photogrammetric measurement of vertical bridge deflection. J. Bridge Eng. 8, 212–222.

Ko, J., Ni, Y., 2005. Technology developments in structural health monitoring of large-scale bridges. Eng. Struct. 27, 1715–1725.

Lazecky, M., Hlavacova, I., Bakon, M., Sousa, J.J., Perissin, D., Patricio, G., 2016. Bridge displacements monitoring using space-borne X-band SAR interferometry. IEEE J. Sel. Top. Appl. Earth Obs. Remote Sens. 10, 205–210.

Liu, X.X., Tong, X., Ding, K., Zhao, X.a., Zhu, L., Zhang, X., 2015. Measurement of long-term periodic and dynamic deflection of the long-span railway bridge using microwave interferometry. IEEE J. Sel. Top. Appl. Earth Obs. Remote Sens. 8, 4531–4538.

Luzi, G., Pieraccini, M., Mecatti, D., Noferini, L., Guidi, G., Moia, F., Atzeni, C., 2004. Ground-based radar interferometry for landslides monitoring: atmospheric and instrumental decorrelation sources on experimental data. IEEE Trans. Geosci. Remote Sens. 42, 2454–2466.

Monserrat, O., Crosetto, M., Luzi, G., 2014. A review of ground-based SAR interferometry for deformation measurement. ISPRS J. Photogramm. Remote Sens. 93, 40–48.

Montazeri, S., Zhu, X.X., Eineder, M., Bamler, R., 2016. Three-dimensional deformation monitoring of urban infrastructure by tomographic SAR using multitrack terraSAR-X data stacks. IEEE Trans. Geosci. Remote Sens. 54, 6868–6878.

Oliver, C., Quegan, S., 1998. Understanding synthetic aperture radar images. Artech House, Boston & London.

Ouchi, K., 2013. Recent trend and advance of synthetic aperture radar with selected topics. Remote Sensing 5, 716–807.

Perissin, D., Wang, Z., Lin, H., 2012. Shanghai subway tunnels and highways monitoring through Cosmo-SkyMed Persistent Scatterers. ISPRS J. Photogramm. Remote Sens. 73, 58–67.

Pieraccini, M., 2013. Monitoring of civil infrastructures by interferometric radar: a review. Scientific World J.

Pieraccini, M., Fratini, M., Parrini, F., Atzeni, C., 2006. Dynamic monitoring of bridges using a high-speed coherent radar. IEEE Trans. Geosci. Remote Sens. 44, 3284–3288.

Pieraccini, M., Fratini, M., Parrini, F., Macaluso, G., Atzeni, C., 2004. High-speed CW step-frequency coherent radar for dynamic monitoring of civil engineering structures. Electron. Lett. 40, 907–908.

Psimoulis, P.A., Stiros, S.C., 2007. Measurement of deflections and of oscillation frequencies of engineering structures using Robotic Theodolites (RTS). Eng. Struct. 29, 3312–3324.

Rödelsperger, S., 2011. Real-time Processing of Ground based Synthetic Aperture Radar (GB-SAR) Measurements. Technische Universität Darmstadt. PhD thesis.

Severin, J., Eberhardt, E., Leoni, L., Fortin, S., 2014. Development and application of a pseudo-3D pit slope displacement map derived from ground-based radar. Eng. Geol. 181, 202–211.

Simons, M., Rosen, P., 2007. Interferometric Synthetic Aperture Radar Geodesy. In: Schubert, G. (Ed.), Treatise on Geophysics. Elsevier Press, pp. 391–446.

Sousa, J., Bastos, L., 2013. Multi-temporal SAR interferometry reveals acceleration of bridge sinking before collapse. Nat. Hazards Earth Syst. Sci. 13, 659–667.

Stabile, T.A., Perrone, A., Gallipoli, M.R., Ditommaso, R., Ponzo, F.C., 2013. Dynamic survey of the Musmeci bridge by joint application of ground-based microwave radar interferometry and ambient noise standard spectral ratio techniques. IEEE Geosci. Remote Sens. Lett. 10, 870–874.

Stilla, U., Soergel, U., Thoennessen, U., 2003. Potential and limits of InSAR data for building reconstruction in built-up areas. ISPRS J. Photogramm. Remote Sens. 58, 113–123.

Strozzi, T., Werner, C., Wiesmann, A., Wegmuller, U., 2012. Topography mapping with a portable real-aperture radar interferometer. IEEE Geosci. Remote Sens. Lett. 9, 277–281.

Tarchi, D., Ohlmer, E., Sieber, A., 1997. Monitoring of structural changes by radar interferometry. J. Res. Nondestructive Eval. 9, 213–225.

Touzi, R., Lopes, A., Bruniquel, J., Vachon, P.W., 1999. Coherence estimation for SAR imagery. IEEE Trans. Geosci. Remote Sens. 37, 135–149.

Voytenko, D., Dixon, T.H., Howat, I.M., Gourmelen, N., Lembke, C., Werner, C.L., De La Peña, S., Oddsson, B., 2015. Multi-year observations of Breiðamerkurjökull, a marine-terminating glacier in southeastern Iceland, using terrestrial radar interferometry. J. Glaciol. 61, 42–54.

Werner, C., Strozzi, T., Wiesmann, A., Wegmüller, U., 2008. Gamma's portable radar interferometer. Proceedings of 13th FIG Symposium on Deformation Measurment and Analysis & 14th IAG Symposium on Geodesy for Geotchnical and Structural Engineering, Lisbon, Portugal, 12–15 May, pp. 1–10.

Werner, C., Wiesmann, A., Strozzi, T., Kos, A., Caduff, R., Wegmiuler, U., 2012. The GPRI multi-mode differential interferometric radar for ground-based observations. 9th European Conference on Synthetic Aperture Radar, Nuremberg, Germany, 23–26 April, pp. 304–307.

Wong, K.Y., 2004. Instrumentation and health monitoring of cable-supported bridges. Struct. Control Health Monit. 11, 91–124.

Wong, K.Y., 2007. Design of a structural health monitoring system for long-span bridges. Struct. Infrastruct. Eng. 3, 169–185.

Xu, Y.L., Xia, Y., 2011. Structural Health Monitoring of Long-span Suspension Bridges. Spon Press, New York.

Zhang, B.C., Ding, X.L., Jiang, M., Zhang, B., Wu, S.B., Liang, H.Y., 2016. Ground-based interferometric radar for dynamic deformation monitoring of the Ting Kau Bridge in Hong Kong. In: Proceeding of the IEEE International Geoscience and Remote Sensing Symposium (IGARSS 2016), Beijing, China, 10–15 July, pp. 6875–6878.

Zhang, L., Ding, X.L., Lu, Z., 2011. Ground settlement monitoring based on temporarily coherent points between two SAR acquisitions. ISPRS J. Photogramm. Remote Sens. 66, 146–152.

Zhong, P., Ding, X.L., Zheng, D., Chen, W., Huang, D., 2008. Adaptive wavelet transform based on cross-validation method and its application to GPS multipath mitigation. GPS Solut. 12, 109–117.

Zogg, H., Ingensand, H., 2008. Terrestrial laser scanning for deformation monitoring-load tests on the felsenau viaduct (CH). The International Archives of the Photogrammetry, Remote Sensing and Spatial Information Sciences, Beijing, China, 3–11 July, pp. 555–562.